24

Minimally invasive force sensing for tendon-driven robots

Alberto Cavallo, Giuseppe De Maria, Ciro Natale and Salvatore Pirozzi
Dipartimento di Ingegneria dell'Informazione, Seconda Università degli Studi di Napoli Aversa (CE), 81031, Italy

1. Introduction

The purpose of this chapter is to present a sensor solution for measurement of tendon tension or joint torque in force control applications of tendon-driven robots. In the robotics community, it is well-known that the use of torque sensors is useful not only when joint friction is significant (Pfeffer et al., 1989), (Vischer & Khatib, 1995), but also when motion or impedance control of flexible joints robots is in order (Ott et al., 2003), (Ott et al., 2004). This is the case, for example, of lightweight robots used for space applications (Ferretti et al., 2005). But probably the most important field of application of torque sensors is the control of robotic hands, in fact such complex systems are specifically designed to allow the robot to interact with the environment, usually unstructured and so generic that a safe interaction can be ensured only if the mechanism possesses a compliant behaviour. When integrated robotic hands are considered (Butterfaß et al., 2001), such compliance has to be provided by torque control (Liu et al., 1999), and therefore finger joint torque sensors appear mandatory. The same objective exists for tendon-driven artificial hands which are the most used solutions for prosthetic applications (Carrozza et al., 2005) and when the torque control could be useful not only for overcoming friction and other disturbances but specifically also for reproducing nonlinear characteristic of human-like tendons (Gialias & Matsuoka, 2004). Since the first prototypes of robotic hands (Salisbury & Craig, 1982), it was clear how important were the requirement of limited invasiveness for every kind of sensor to be integrated into the device. From the first solutions provided for tendon-driven fingers (Kaneko et al., 1990) only limited progress has been made and the sensor solutions adopted appear still cumbersome and quite invasive (Jung et al., 2007). These are usually based on strain gauges, which are cumbersome and require additional mechanical components and interfaces in order to provide the necessary measurement (Biagiotti et al., 2005).
The alternative solution described in this chapter is based on a Fibre Bragg Grating (FBG) used as strain sensor. Owing to the minimally invasive nature typical of optical fibres, it can be easily integrated in any type of tendon-driven robot. One of the most promising applications can be the integration of the sensor into anthropomorphic robotic hands for accurate impedance or compliance control. The sensing element of the proposed torque sensor can be easily bonded directly to the tendon following its natural routing with a significantly reduced invasiveness with respect to conventional sensors. In fact, the Bragg

sensor is embedded into the optical fibre whose typical diameter is about 125μm which allows its integration into the tendon itself. Furthermore, the greatest advantage of a solution based on the FBG, bonded directly to the tendon, is its immunity to electromagnetic disturbances typical of optical fibres, and thus it can be used without any concern in conjunction with the electrical motors, usually adopted for robotic actuation, even in close vicinity as it happens for robotic hands.

The experimental results presented here have been obtained on a simple test-bench realized by using off-the-shelf and cheap components conceived to demonstrate the potentiality of the sensor and its effectiveness in an actual compliance control scheme of a single-joint mechanism. In such type of control schemes, it is of major importance to ensure that the actuator exerts on the tendon a prescribed force or a prescribed torque when pulleys are used for mechanism actuation. The main limiting factor in achieving such a goal is the presence of dry friction at motor side, especially in the gear trains usually adopted to optimize torque transfer from the motor to the tendon. As mentioned before, such limitation can be easily overcome by means of torque or force feedback. In the experimental setup used here, the fibre has been bonded to a steel tendon with a diameter of 420 μm used to drive the servomechanism built to emulate a single articulation of a tendon-driven robot. The optical sensor measures the strain variation that an external torque generates on the tendon. Two different demodulations schemes are compared, i.e. a conventional narrowband (Zhao & Liao, 2004) and a new modified broadband interrogation circuit are implemented to convert the optical signal into an electrical one. For each demodulation scheme, the sensor has been calibrated using load cells and the differences between the two schemes have been highlighted in terms of sensitivity and dynamic range.

Taking into account the requirements of the implemented compliance control system, one of the two demodulation schemes has been implemented in the real feedback control application to evaluate the quality and the effectiveness of the proposed sensor.

The chapter is organized as follows. Section 2 presents the working principle of the optoelectronic sensor together with the two demodulation schemes designed as conditioning electronics. In Section 3, the sensor calibration curves are measured for both demodulation schemes with a suitable experimental apparatus using precision load cells. Section 4 reports the experimental results of the exploitation of the proposed tension sensor in an actual feedback control law, i.e. a compliance control of a single-joint mechanism actuated through a steel tendon.

2. Optical tension sensor based on FBG

As already mentioned, the basic idea is to exploit the FBG as a strain sensor since such a strain is proportional to the tendon tension through the elasticity of the tendon itself. Therefore, to improve sensor sensitivity, loss of strain transfer from the tendon to optical fibre has to be avoided. To this aim, before bonding the FBG to the steel tendon, the portion of fibre jacket corresponding to the grating position was removed. A picture reporting a detail of the optical sensor is presented in Fig. 1, where it is evident how minimally invasive is the sensing element.

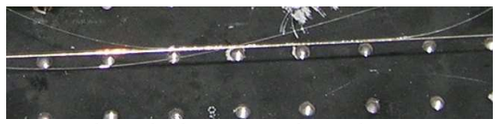

Fig. 1. Detail of the Bragg grating bonded to a steel tendon.

It is well-known that when the FBG is subject to a strain, its reflectivity spectrum shifts and thus a suitable conditioning electronics can be used to detect such a shift converting it into an electrical signal. The most common demodulation technique is based on the acquisition of the whole grating reflectivity spectrum through an optical spectrum analyzer detecting the shift of its peak (Zhao & Liao, 2004). However, such solutions are charaterized by relatively long response time and thus can be used to measure static and slowly varying dynamic strains. Also, the conditioning electronics used to implement such techniques is quite complex, cumbersome and expensive. In other applications, like in force measurement in robotics, the needed response time is significantly lower and, at the same time, simple, cheap and with limited weight and size electronics are desireble. Therefore, different demodulation techniques are mandatory, like those presented in the following.

2.1 Narrow band demodulation

The first technique presented to interrogate the proposed sensor is based on a narrow-band demodulation scheme. The output light wave from a single longitudinal mode Distributed FeedBack (DFB) diode laser was used to probe the wavelength shift of the FBG reflection curve imposed by the strain signal to be detected. If the laser frequency is within the linear range of the FBG reflection slope, the strain signals will change the reflected power, which can be simply measured using a photodetector (Zhao & Liao, 2004). It can be seen that this technique has several advantages, such as fast response, ease of use and high sensitivity depending on leading edge slope of the FBG reflection curve. The reflectivity spectrum of the FBG used in our experiments had a quasi-flat top from 1552 nm to 1556 nm, with a peak reflectivity ≥ 75% (see Fig 2). The leading edge of the FBG reflection curve extended from 1547.28 nm to 1550.95 nm (measured from 10% to 90% of maximum reflectivity), whereas the right portion extended from 1556.37 nm to 1557.24 nm. The trailing edge of the FBG reflection slope allowed for a 72GHz linear slope width, and it was chosen as the operating range due to the higher linearity exhibited by the FBG reflectivity in this spectral portion. In order to keep a linear relationship between the reflected optical power and the strain signal, the DFB laser emitting wavelength must lie within the trailing edge of the FBG reflectivity spectrum (see Fig. 2). Moreover, assuming a typical FBG curve shift of 1 nm for an applied strain of 1000 με (Kersey et al., 1997), the strain level must be kept lower than 870 με in order to avoid sensor output saturation.

The optical set-up employed for FBG interrogation is schematically illustrated in Fig. 3. Light emitted by a DFB laser was sent to a Y-coupler, which directed the light to the FBG. Light reflected from the FBG was then re-directed to a photodiode, whose bandwidth was on the order of hundreds of MHz, thus much higher than the bandwidth of the strain signals to be detected. The output signal from the photodiode was finally sent to the conditioning electronics, basically formed by a low-pass filter used to eliminate the high-frequency noise.

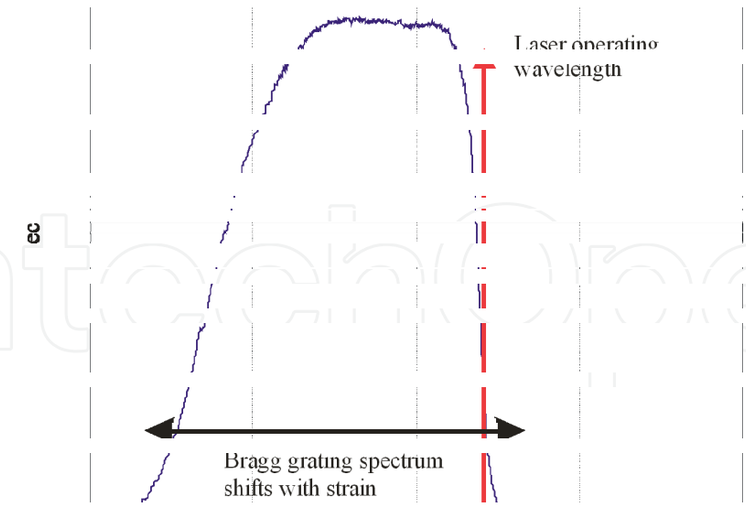

Fig. 2. Reflectivity spectrum of the grating.

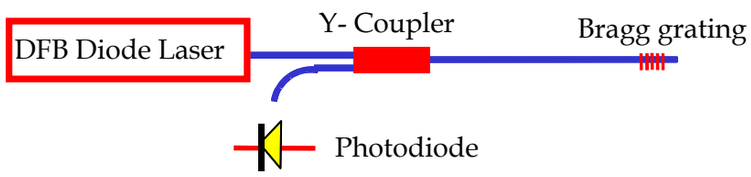

Fig. 3. FBG narrow band demodulation scheme.

2.2 Broadband demodulation

The second technique presented to interrogate the proposed sensor uses the Bragg grating together with a broadband SLED optical source. Differently from classical demodulation techniques using a broadband source, the technique proposed here is not based on a spectral analysis and thus allows to measure fast varying dynamic strain. The output light of SLED was used to illuminate the FBG, which presents a very narrow spectrum compared to that of the source. If the strain signal to be detected shifts the Bragg grating reflection curve within a monotonous range of the broadband source spectrum, the variations of the reflected power can be simply measured using a photodetector (see Fig. 4). With respect to the technique described in the previous subsection this one shows the same advantages in terms of fast response and ease of use. In this case, the sensitivity depends both on leading edge slope of the SLED spectrum and on Bragg grating reflection curve. Depending on the application requirements an optimal combination of these parameters can be selected. Moreover, the maximum strain level measurable with this technique is limited only by the maximum applicable deformation before the breaking of the grating (about 10000 με). In fact, a strain level of 10000 με corresponds to a FBG spectrum shift of about 10 nm which is well below the length of the broadband source leading edge that is about 50 nm. The

reflectivity spectrum of the FBG used in our experiments for this demodulation technique had a peak reflectivity ≥ 90% and a full-width-half-maximum bandwidth of 0.168 nm with a centre wavelength of 1520.132 nm. The optical set-up employed for broadband interrogation is essentially similar to the narrow band case with the broadband source instead of DFB laser (see Fig. 5). Light emitted by broadband source was sent to a Y-coupler, which directed the light to the FBG. Light reflected from the FBG was then re-directed to the photodiode connected to the conditioning electronics. Moreover, the cost and the encumbrance of this solution are lower since the DFB diode laser is more expensive and more cumbersome with respect to the SLED source.

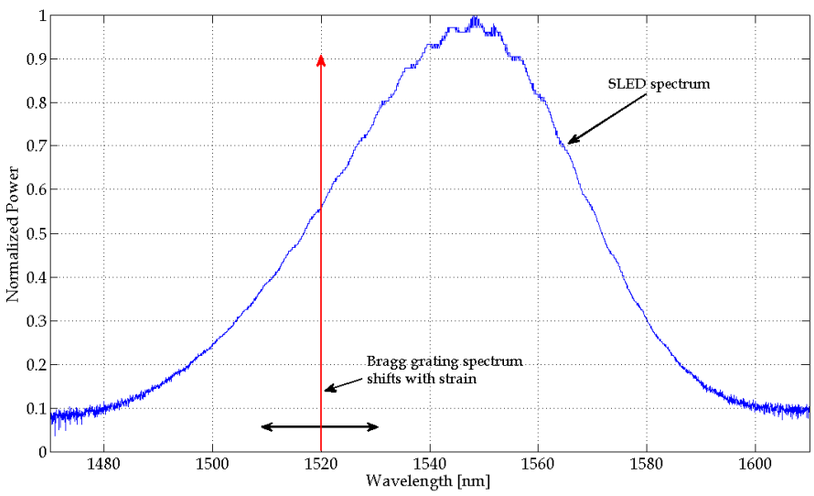

Fig. 4. Spectrum of broadband source with respect to the FBG.

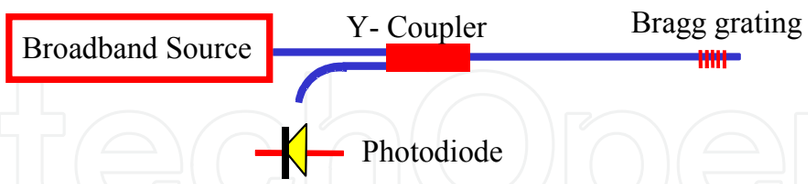

Fig. 5. FBG broadband demodulation scheme.

3. Sensor calibration

The force sensor has been calibrated using a setup constituted by a steel tendon with a diameter of 250 μm connected, at one end, to a micro-positioning stage and to a load cell used to calibrate the tension sensor, at the other end (Fig. 6). When the micro-positioning stage moves, a force causes a strain variation of the tendon proportional to the stiffness of the material used to realize the tendon. The FBG measures this strain and consequently the

tension after a proper calibration procedure. The force f is related to the output voltage v_B obtained from the optical sensor signal after the demodulation and a suitable electronic conditioning as

$$f = k_s k_\varepsilon v_B = k_B v_B \quad (1)$$

where k_ε is the strain sensitivity, and k_s is the tendon stiffness sketched as a lumped spring in Fig. 7, being k_B the overall sensor sensitivity. During the calibration of the sensor, the force applied to the tendon, shown as f in Fig. 7, has been measured using a load cell and the corresponding output voltage v_B of the conditioning electronic circuit has been evaluated.

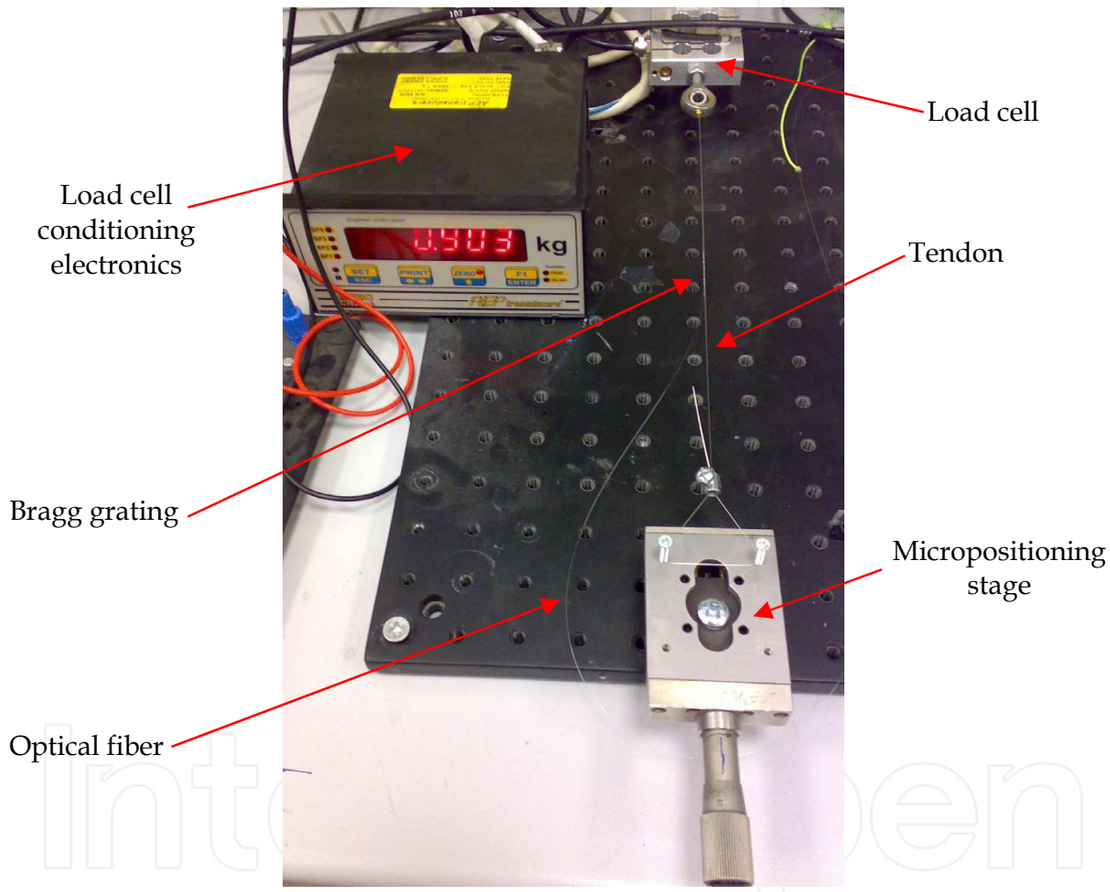

Fig. 6. Picture of the calibration setup

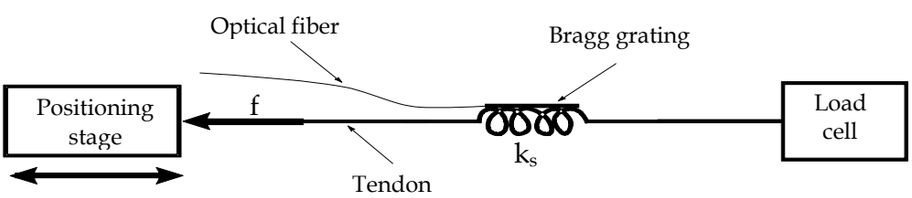

Fig. 7. Sketch of the calibration setup.

The same setup has been used to calibrate the sensor using the two demodulation techniques described above. Different set of experimental measurements has been carried out to calibrate the optical sensor in the two cases. The measurements have been fitted with a linear curve, whose parameters have been estimated with a least mean square algorithm. Fig. 8 shows the results of the sensor calibration with a narrow band demodulation technique reporting the experimental data and the fitting curve, whose equation is

$$f = 2.61 v_B + 0.11 \tag{2}$$

The calibration curve and the fitting curve of the sensor with a broadband demodulation technique is reported in Fig. 9. In this case the equation of fitting curve is

$$f = 46.78 v_B + 0.54 \tag{3}$$

The constant offset term in both cases, due to sensor electronics, and reported in (2),(3) can be easily eliminated via software whenever a digital control system is adopted to exploit the sensor measurement. In conclusion, the Bragg sensor used with a narrow band demodulation technique can be considered a force transducer with a calibration constant of 2.61 N/V, while with a broadband demodulation technique the calibration constant is 46.78 N/V.

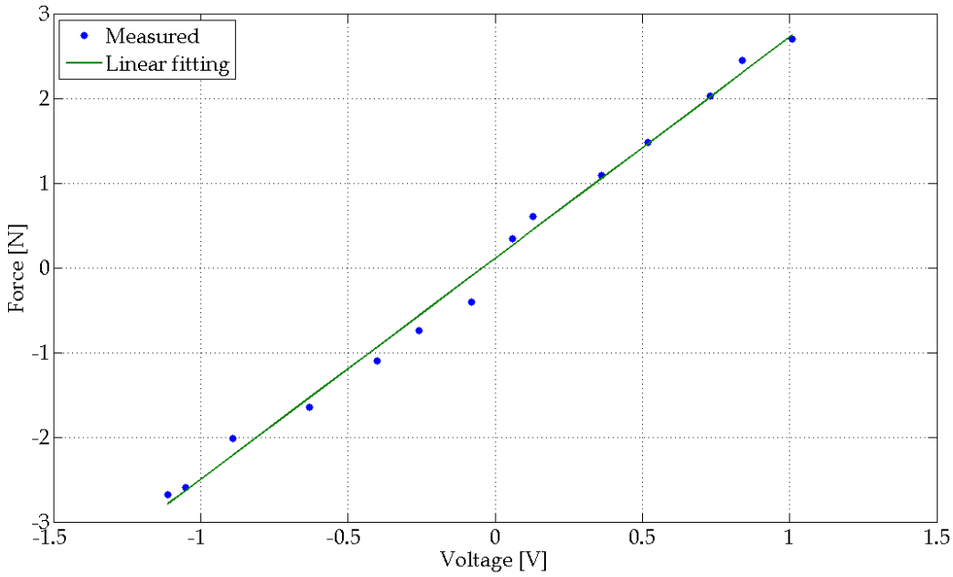

Fig. 8. Calibration curve with narrow band demodulation.

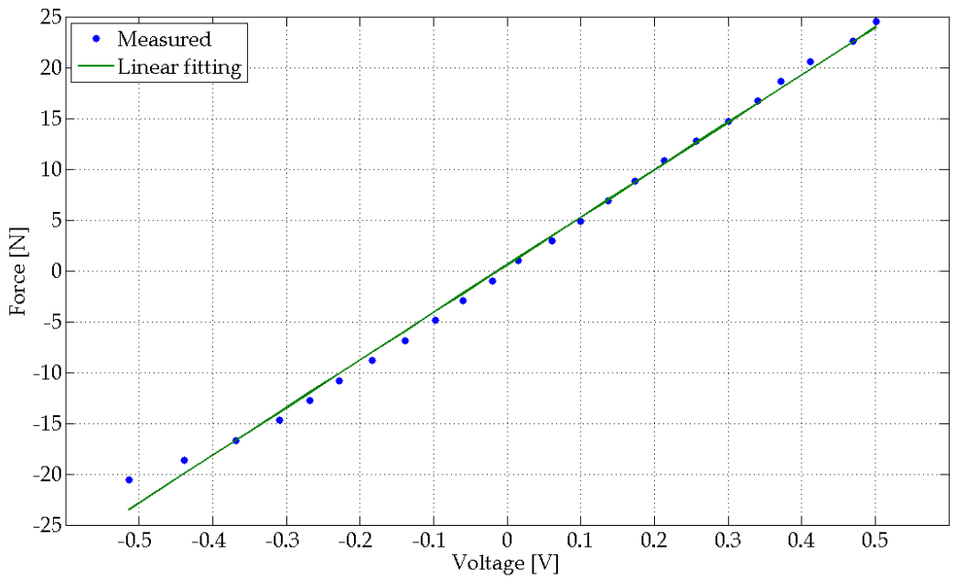

Fig. 9. Calibration curve with broadband demodulation.

4. Testing

The test-bench, whose picture is reported in Fig. 10, is constituted by a steel tendon stretched between two pulleys. The first one is connected via gear train with the motor shaft (left side of the picture), the other pulley is fixed to the inertial load (right side of the picture). The load shaft is connected to the supporting structure through ball bearings to reduce the load-side friction as much as possible. In fact, one of the expected results of the force feedback is to counteract the disturbances (mainly dry friction) acting only on the motor side, while no rejection of load-side disturbances is expected. A potentiometer is mounted to the motor side in order to measure angular position for implementation of compliance control. The Bragg sensor written into the optical fibre is bonded to the tendon and a conditioning electronics module, based on the narrow band technique (see Section 3), has been designed and produced to suitably demodulate the optical output signal. The implemented solution has been selected taking into account the range within the force amplitudes vary during the testing.

4.1 Test-bench Mathematical Modelling

The test-bench described so far can be schematically represented as in Fig. 12 where the tendon stiffness is sketched as a lumped spring. The mathematical model of the proposed test-bench is the classical two-mass system whose equations are

$$J_m\ddot{\vartheta}_m + \beta_m\dot{\vartheta}_m = k_r k_t i_m - \tau_l - \tau_d \tag{4}$$

$$J_l\ddot{\vartheta}_l + \beta_l\dot{\vartheta}_l = \tau_l + \tau_e \tag{5}$$

$$\tau_l = 2rk_s(\vartheta_m - \vartheta_l)r \tag{6}$$

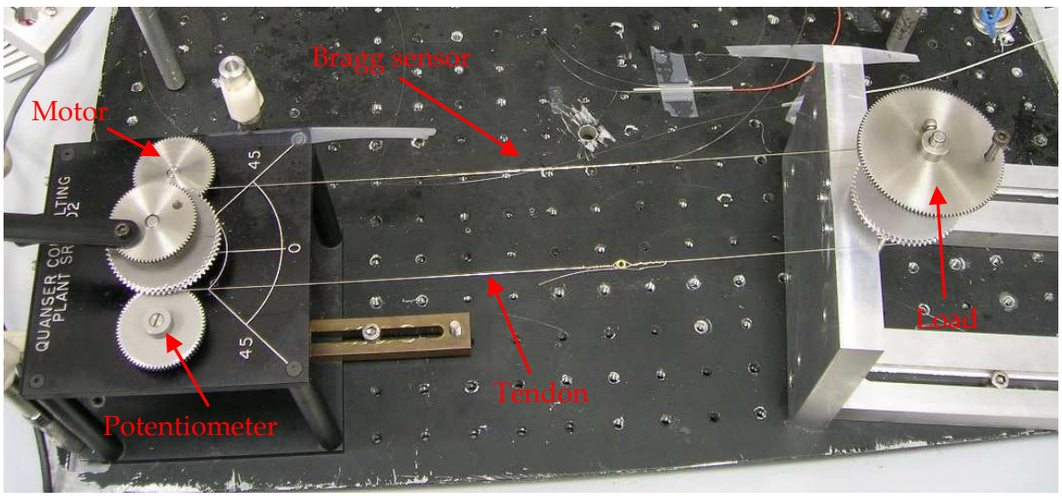

Fig. 10. Test bench setup for testing.

where J_m, β_m, ϑ_m and J_l, β_l, ϑ_l are the overall inertia, friction coefficient and angular position of the motor side and load side respectively. The motor is driven by the armature current i_m with torque constant k_t, and it is connected to the pulley via gear train with gear ratio k_r. Both pulleys have diameter 2r and the tendon stiffness is k_s. The load torque τ_l is the torque transferred to the load through the tendon, which has been suitably prestressed in order to prevent buckling thus allowing measurement of both positive and negative torques. The disturbance torque τ_d takes into account all the dynamic effects not explicitly modelled, e.g. dry friction and high frequency dynamics. Finally, τ_e represents the external torque applied to the load which models the interaction of the servomechanism with the environment. If a load torque is applied to the system the tendon exhibits a strain variation proportional to the stiffness of the material used to realize the tendon. Using the presented sensor, it is possible to measure this strain and consequently the load torque after a proper calibration procedure. The narrow band demodulation technique has been selected considering the maximum strain that the implemented setup exerts on tendon.

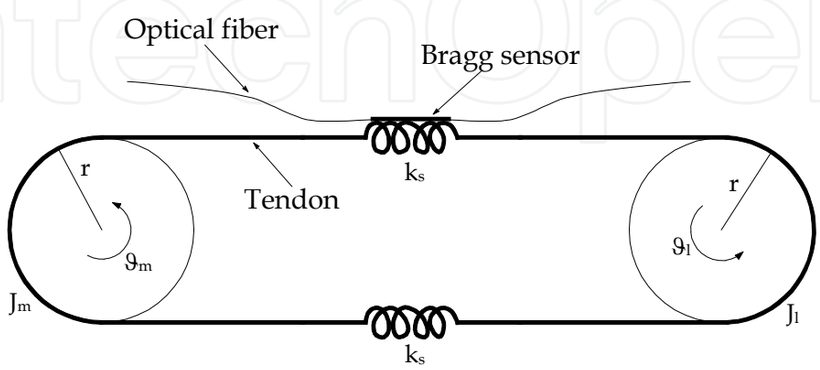

Fig. 11. Sketch of the test bench.

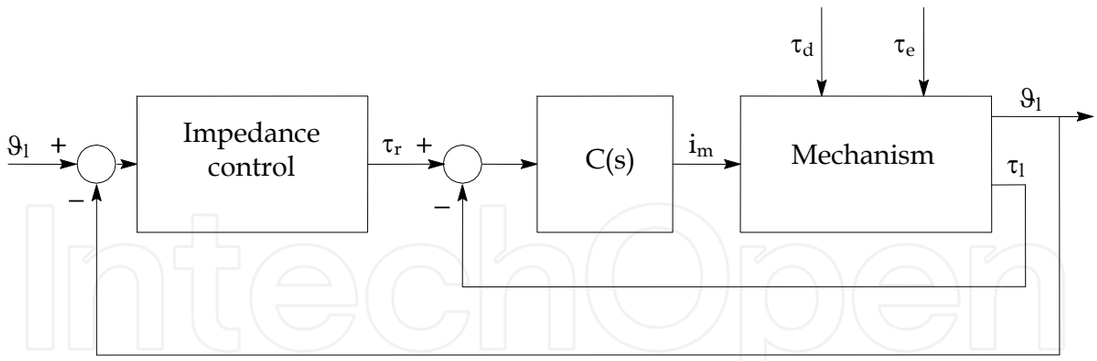

Fig. 12. Compliance control scheme.

4.2 Compliance Control

The compliance control system used to test the proposed torque sensor is based on a double control loop, a typical control scheme reported in the literature (see Fig. 12). The control input of the mechanical system is the motor driving current i_m, while the measured outputs are the angular position ϑ_l and the load torque τ_l. The unmanipulable inputs of the system are the disturbance torque τ_d and the external torque τ_e. The torque controller C(s) operates so as to reduce the error between the reference torque τ_r and the measured load torque. The reference torque is generated by the outer compliance controller evaluating the error between the reference angular position ϑ_r and the actual angular position ϑ_l. The performances of a compliance or an impedance control broadly depend on the disturbances at motor torque level and the objective of the torque inner controller is to reject the disturbance τ_d.

Taking into account the mathematical model of the mechanism, reported in (4),(5) and that the main source of torque disturbances is constituted by the Coulomb friction, i.e. a constant friction torque, the torque controller has to include an integral action on the torque error so as to completely reject the constant input disturbances. The proposed linear controller has transfer function

$$C(s) = \frac{k_c(1+sT_1)}{s(1+sT_2)} \frac{1+s2\zeta/\omega_n + s^2/\omega_n^2}{(1+sT_3)^2} \tag{7}$$

where k_c is the controller gain and the time constants T_1 and T_2 are chosen such that $T_1 > T_2$ resulting into a phase-lead term aimed at ensuring the stability of the closed-loop system. In order to improve the performance in terms of bandwidth, and thus tracking accuracy, a couple of complex zeros is introduced to avoid that the closed-loop resonant mode related to the flexible connection between the motor and the load gets unstable. Finally, two high frequency poles with the same time constant T_3 have been introduced to keep a sufficient roll-off of the loop gain to filter measurement noise.

The compliance control law of outer loop computes τ_r as

$$\tau_r = k_p(\vartheta_r - \vartheta_l) - k_d\dot{\vartheta}_l + \beta_l\dot{\vartheta}_l \tag{8}$$

and, under the assumption of perfect tracking of the inner loop, i.e. $\tau_l = \tau_r$, the closed-loop system behaviour is described by the equation

$$J_l\ddot{\vartheta}_l + k_d\dot{\vartheta}_l + k_p(\vartheta_l - \vartheta_r) = \tau_e \tag{9}$$

where the user can select the desired stiffness value k_p and the desired friction parameter k_d.

4.3 Experimental results

Two different sets of experiments have been carried out to compare both the static and the dynamic performance of the compliance control making use the proposed torque sensor with those of a compliance control implemented with the sole position feedback. Note that in both cases, the load angular position used in the outer loop controller has not been measured directly, but it has been considered equal to the motor angular position measured through the potentiometer as in Fig. 10, under the assumption of a reference position ϑ_r with significant spectral components within a frequency range much lower than the resonant mode of the system. In the case of pure position feedback, the torque inner loop has been replaced with the transfer function

$$C_F(s) = \frac{1}{k_r k_t(1+sT)} = \frac{1}{14 \cdot 0.00767(1+s/200)} \tag{10}$$

which transforms the reference torque τ_r, computed by the compliance controller (8), into the motor driving current i_m by taking into account both the gear ratio k_r and the torque constant k_t in (4) and by filtering high frequencies with the same roll-off of the torque loop gain.

A set of static measurements has been made to compare the actual stiffness to the desired one when the pure position feedback is implemented. In detail, with different values of k_p, several values of external torque τ_e have been applied to the system and the corresponding position ϑ_l has been measured so as to estimate the actual stiffness k_{pa} of the servomechanism via a least-mean square method. The desired and actual stiffness values are reported in Table 1 together with the relative error defined as

$$e_{\%} = 100\frac{k_{pa} - k_p}{k_p} \tag{11}$$

The table evidently shows how the performance of the pure position control approach is quite limited for low values of desired stiffness, while it improves for higher values of desired stiffness.

k_p [Nm/rad]	0.100	0.200	0.300	0.400	0.500
k_{pa} [Nm/rad]	0.131	0.212	0.328	0.484	0.502
$e_{\%}$	31.3	6.17	9.44	21.0	0.406

Table 1. Actual servomechanism stiffness without torque feedback

k_c [A/Nm]	T_1 [s]	T_2 [s]	ζ	ω_n [rad/s]	T_3 [s]
250	1/5	1/50	0.025	$2\pi 180$	1/2200

Table 2. Parameters of the controller C(s)

As expected, when the torque feedback is used, with the parameters selected for the torque controller C(s) in (7) as reported in Table 2, the error in (11) is zero for every value of desired stiffness, since the pole in the origin of C (s) ensures a null tracking error at steady-state.
A second set of experiments has been performed to evaluate the dynamic characteristics of the compliance control obtained with the proposed control system. Then, the actual dynamic behaviour is compared with both the desired one and with that achieved using the pure position feedback.
A square-wave reference position ϑ_r with a frequency of 0.5Hz has been imposed to the system and experiments have been carried out with different values of k_p and of k_d. First of all, the load inertia J_l has been estimated using the torque controller as described in the following. Several couples of values for k_d and k_p have been imposed so as to obtain lightly damped responses and then natural frequencies ω_n have been evaluated from the analysis of the transient responses in terms of load position. With reference to (9), the actual value of the stiffness is equal to the imposed one owing to the torque control action, thus, the inertia J_l can be computed as k_p/ω_n^2 for each experiment. Eventually, the mean value has been chosen as the estimated value of the load inertia, namely $J_l = 10^{-4}$ Nms^2/rad. Therefore, by knowing the impedance parameters J_l, k_d and k_p, it is possible to calculate the theoretical dynamic response of the load position and compare it with the actual response of the system under the compliance control.
The results when torque feedback control is implemented with impedance parameters $k_d=10^{-3}$ and $k_p = 0.1$ are reported in Fig. 13 displaying the reference angular displacement ϑ_r together with the angular displacement (desired ϑ_l) computed from the theoretical equation (9) and the actual one. It is evident that the natural frequency and the settling time of the experiment are very close to the theoretical ones, even though the two curves are not identical due to some residual nonlinearities, which can mainly be attributed to friction disturbances acting on the load shaft, against which the torque loop has no effect. Similar remarks can be made for the results shown in Fig. 14, where the same test is reported for different values of the impedance parameters $k_d = 8\cdot10^{-3}$ and $k_p = 0.1$ leading to a damped response. In such a case, the non null steady-state error is due to the effect of dry friction on the load shaft. The same two experiments have been repeated when the compliance control, with the same impedance parameters k_p and k_d, using only position feedback is implemented. The results are shown in Fig. 15 and Fig. 16, and it is evident how different from the expected one is the poor dynamic performance obtained with this approach, in fact in both cases a highly damped response as well as a large steady-state error are obtained due to the effect of friction acting on the motor and gear shafts.

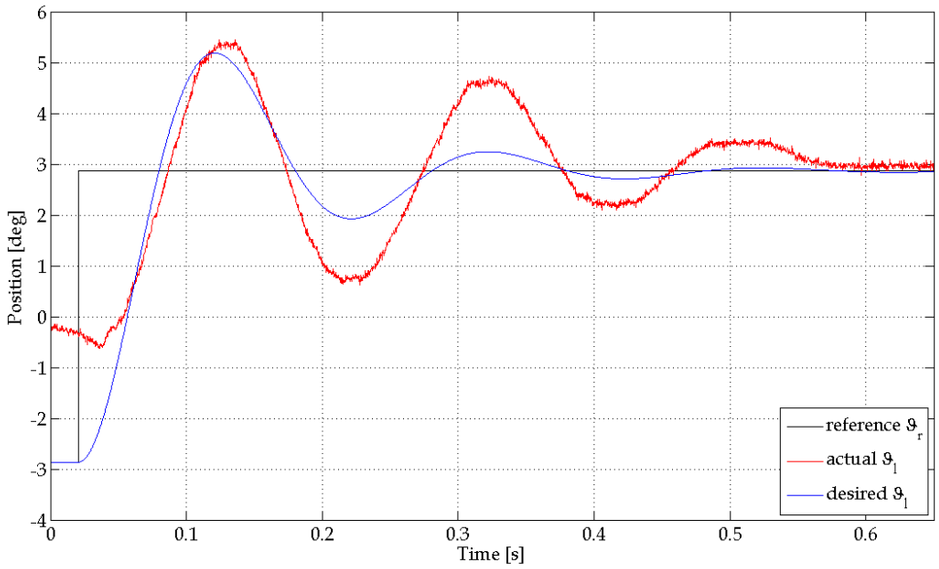

Fig. 13. Compliance control with position and torque feedback ($k_d=10^{-3}$ and $k_p=0.1$)

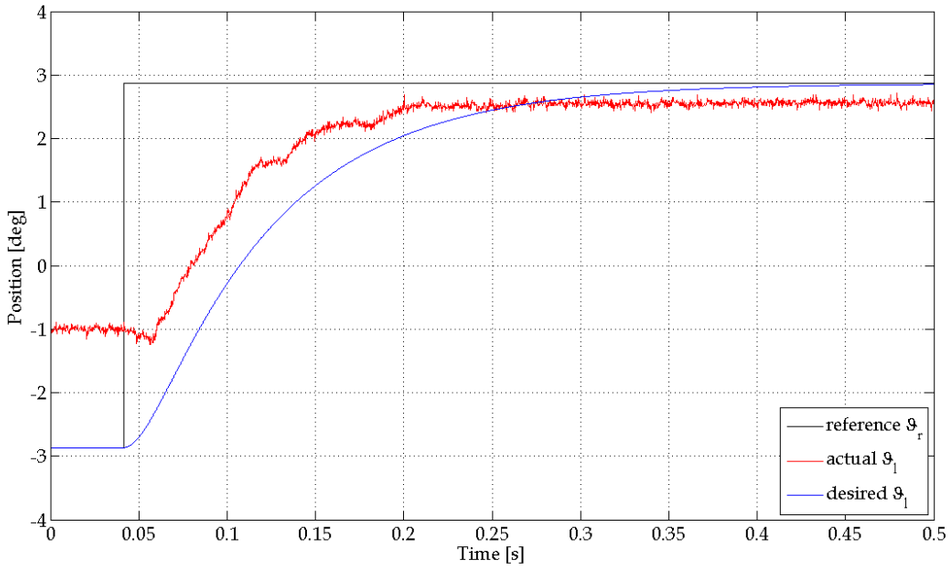

Fig. 14. Compliance control with position and torque feedback ($k_d=8\cdot10^{-3}$ and $k_p=0.1$)

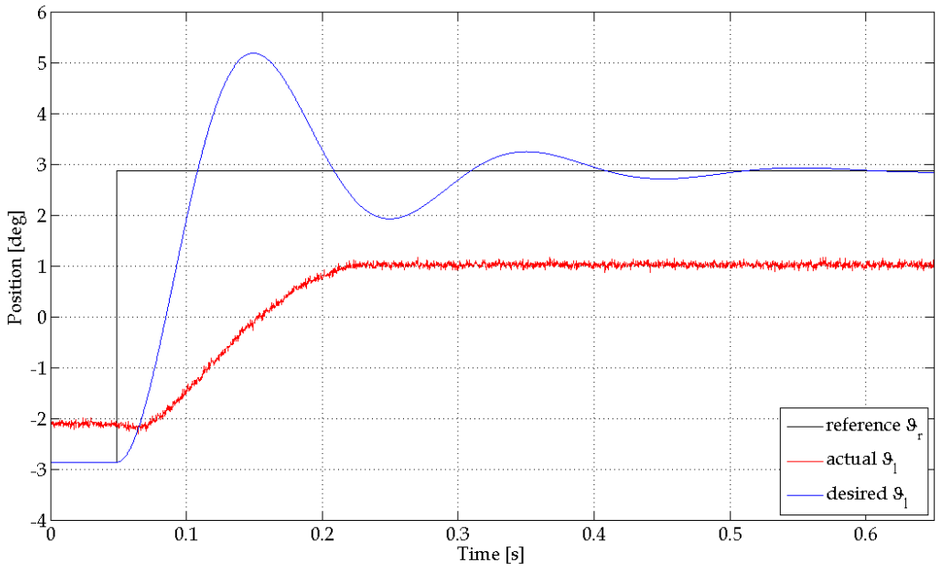

Fig. 15. Compliance control with only position feedback (k_d=10^{-3} and k_p=0.1)

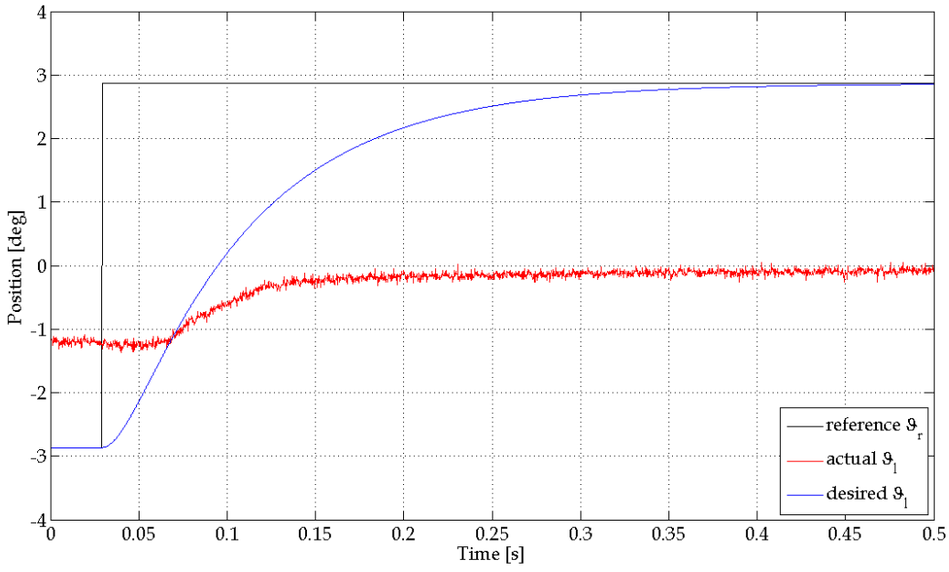

Fig. 16. Compliance control with only position feedback (k_d=$8 \cdot 10^{-3}$ and k_p=0.1)

5. Conclusions

The chapter tackles the problem of the design of a sensor to measure the tendon tension for tendon-driven robots. The requirements of this application are the minimally invasiveness of the sensing element itself and the limited complexity, weight, cost and size of the conditioning electronics. The proposed solution is based on optoelectronic technology, i.e. a

FBG used as force sensor. Such a choice permits to satisfy the minimally invasiveness requirement since the grating is integrated into a fibre of sole 125 μm and can be directly bonded to the tendon. Two different demodulation schemes have been proposed to be selected according to application requirements in terms of dynamic range and sensitivity. Both techniques allow to measure fast varying dynamic strain in contrast to classical demodulation schemes based on spectral analysis. Moreover, the second one can be implemented with cheaper optoelectronic components and with lighter conditioning electronics. The two schemes have been implemented for the realization of two tendon tension sensors with different calibration curves, which have been experimentally identified. Finally, the sensor interrogated using the narrow band demodulation technique has been exploited as a torque feedback sensor in a compliance control system of a single joint mechanism. The experimental results showed the advantage provided by torque feedback when a highly compliant behaviour is required to the servomechanism without losing position tracking performance.

6. Acknowledgement

The research leading to these results has received funding from the European Community's Seventh Framework Programme (FP7/2007-2013) under grant agreement no. 216239 (DEXMART project).

7. References

Biagiotti, L.; Lotti, F.; Palli, G.; Tiezzi, P.; Vassura, G. & Melchiorri, C. (2005). Development of UB Hand 3: Early Results, *Proc. of IEEE Int. Conference on Robotics and Automation*, pp. 4488-4493, Barcelona.

Butterfaß, J.; Grebenstein, M.; Liu, H. & Hirzinger, G. (2001). DLR-Hand II: Next Generation of a Dextrous Robot Hand, *Proc. of IEEE Int. Conf. on Robotics and Automation*, pp. 109-114, Seoul.

Carrozza, M. C.; Cappiello, G.; Stellin, G.; Zaccone, F.; Vecchi, F.; Micera, S. & Dario, P. (2005). On the Development of a Novel Adaptive Prosthetic Hand with Compliant Joints: Experimental Platform and EMG Control, *Proc. of IEEE/RSJ Int. Conference Intelligent Robots and Systems*, pp. 1271-1276, Edmonton.

Ferretti, G.; Magnani, G.; Viganò, L. & Rusconi, A. (2005). On the use of torque sensors in a space robotics application, *Proc. of IEEE Int. Conference on Robotics and Automation*, pp. 1947–1952, Edmonton.

Gialias, N. & Matsuoka, Y. (2004). Muscle Actuator Design for the ACT Hand, *Proc. of IEEE Int. Conference on Robotics and Automation*, pp. 3380–3385, New Orleans.

Jung, S. Y.; Kang S. K.; Lee, M. J. & Moon, I. (2007). Design of Robotic Hand with Tendon-driven Three Fingers, *Proc. of IEEE International Conference on Control and Automation*, pp. 83-86, Seoul.

Kaneko, M.; Yokoi, K. & Tanie, K. (1990). On a New Torque Sensor for Tendon Driven Fingers, *IEEE Tranactions on Robotics and Automation, 6* (4), pp. 501-507.

Kersey, A. D.; Davis, M. A.; Patrik, H. J.; LeBlanc, M.; Poo, K. P.; Askins, A. G.; Putnam, M. A. & Friebele, E. J. (1997). Fiber grating sensors, *Journal of Lightw. Technol. , 15* (8), pp. 1442-1462.

Liu, H.; Butterfaß, J.; Knoch, S.; Meusel, P. & Hirzinger, G. (1999). A new control strategy for DLR's multisensory articulated hand, *Control Systems Magazine , 19* (2), pp. 47-54.

Ott, C.; Albu-Schaffer, A.; Kugu, A. & Hirzinger, G. (2003). Decoupling based Cartesian impedance control of flexible joint robots, *Proc. of IEEE Int. Conference on Robotics and Automation*, pp. 3101–3107, Taipei.

Ott, C.; Albu-Schaffer, A.; Kugu, A.; Stramigioli, S. & Hirzinger, G. (2004). A passivity based Cartesian impedance controller for flexible joint robots Part I: torque feedback and gravity compensation, *Proc. of IEEE Int. Conference on Robotics and Automation*, pp. 2659–2665, New Orleans.

Pfeffer, L.; Khatib, O. & Hake, J. (1989). Joint Torque Sensory Feedback in the Control of a PUMA Manipulator, *IEEE Tran. on Robotics and Automation , 5* (4), pp. 418-425.

Salisbury, J. & Craig, J. (1982). Articulated Hands: Force Control and Kinematic Issues, *Int. J. of Robotic Research , 1* (1), pp. 4-17.

Vischer, D. & Khatib, O. (1995). Design and Development of High-Performance Torque-Controlled Joints, *IEEE Tran. on Robotics and Automation , 11* (4), pp. 537-544.

Zhao, Y. & Liao, Y. (2004). Discrimination methods and demodulation techniques for fiber bragg grating sensors, *Opt. Lasers Eng. , 41*, pp. 1-18.

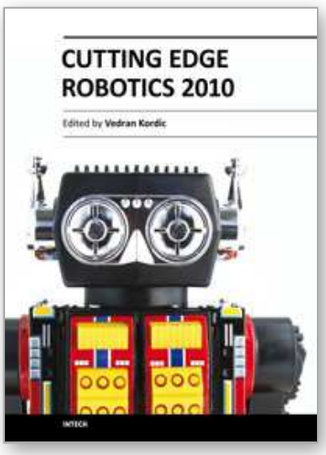

Cutting Edge Robotics 2010

Edited by Vedran Kordic

ISBN 978-953-307-062-9

Hard cover, 440 pages

Publisher InTech

Published online 01, September, 2010

Published in print edition September, 2010

Robotics research, especially mobile robotics is a young field. Its roots include many engineering and scientific disciplines from mechanical, electrical and electronics engineering to computer, cognitive and social sciences. Each of this parent fields is exciting in its own way and has its share in different books. This book is a result of inspirations and contributions from many researchers worldwide. It presents a collection of a wide range of research results in robotics scientific community. We hope you will enjoy reading the book as much as we have enjoyed bringing it together for you.

How to reference

In order to correctly reference this scholarly work, feel free to copy and paste the following:

Alberto Cavallo, Guiseppe De Maria, Ciro Natale and Salvatore Pirozzi (2010). Minimally Invasive Force Sensing for Tendon-driven Robots, Cutting Edge Robotics 2010, Vedran Kordic (Ed.), ISBN: 978-953-307-062-9, InTech, Available from: http://www.intechopen.com/books/cutting-edge-robotics-2010/minimally-invasive-force-sensing-for-tendon-driven-robots

INTECH
open science | open minds

InTech Europe
University Campus STeP Ri
Slavka Krautzeka 83/A
51000 Rijeka, Croatia
Phone: +385 (51) 770 447
Fax: +385 (51) 686 166
www.intechopen.com

InTech China
Unit 405, Office Block, Hotel Equatorial Shanghai
No.65, Yan An Road (West), Shanghai, 200040, China
中国上海市延安西路65号上海国际贵都大饭店办公楼405单元
Phone: +86-21-62489820
Fax: +86-21-62489821

IntechOpen